

RESEARCH ARTICLES

MEMORY

Synaptic mechanisms of pattern completion in the hippocampal CA3 network

Segundo Jose Guzman,¹ Alois Schlögl,¹ Michael Frotscher,² Peter Jonas^{1*}

The hippocampal CA3 region plays a key role in learning and memory. Recurrent CA3–CA3 synapses are thought to be the subcellular substrate of pattern completion. However, the synaptic mechanisms of this network computation remain enigmatic. To investigate these mechanisms, we combined functional connectivity analysis with network modeling. Simultaneous recording from up to eight CA3 pyramidal neurons revealed that connectivity was sparse, spatially uniform, and highly enriched in disynaptic motifs (reciprocal, convergence, divergence, and chain motifs). Unitary connections were composed of one or two synaptic contacts, suggesting efficient use of postsynaptic space. Real-size modeling indicated that CA3 networks with sparse connectivity, disynaptic motifs, and single-contact connections robustly generated pattern completion. Thus, macro- and microconnectivity contribute to efficient memory storage and retrieval in hippocampal networks.

The hippocampal CA3 region plays a key role in learning and memory (1–5). A hallmark property of the network is its ability to retrieve patterns from partial or noisy cues, a process referred to as autoassociative recall, attractor dynamics, or pattern completion (3–7). However, the synaptic mechanisms underlying pattern completion have remained enigmatic. Previous neuronal network models suggested that recurrent CA3–CA3 pyramidal cell synapses play a key role in this process (8–14). In the storage phase, a stimulus pattern will activate an ensemble of interconnected neurons and induce synaptic potentiation in the corresponding recurrent synapses. In the recall phase, a partial pattern will initially activate only a fraction of the ensemble, but subsequently recruit the remaining cells via potentiated synapses. Successful pattern completion requires sufficient synaptic efficacy and network connectivity (12, 14). Whether the biological properties of the CA3 network are consistent with these assumptions remains unclear.

Analysis of functional connectivity in the CA3 network

The CA3 network is often envisaged as a network of highly interconnected neurons (3–5, 8, 11). To test this hypothesis, we analyzed functional connectivity by simultaneous recordings from up to eight CA3 pyramidal neurons in rat brain *in vitro*, followed by selective biocytin labeling (Fig. 1, A to D, and fig. S1). In comparison to recording from sequential pairs, simultaneous recording from the same number of neurons allowed us to test a

much larger number of potential synaptic connections (56 in an octuple configuration versus 8 in four sequential pairs; Fig. 1A). In total, we found 146 synaptic connections in 15,930 pairs tested (in 72 octuple, 66 septuple, 118 sextuple, 120 quintuple, 135 quadruple, 96 triple, and 495 double recordings; 4164 CA3 pyramidal neurons in 1102 slices). The huge majority of interactions were chemical, as demonstrated by block by the AMPA-type glutamate receptor antagonist CNQX; evidence for electrical coupling was found in only 1 out of 15,930 potential connections (fig. S2). Unitary excitatory postsynaptic potentials (EPSPs) had a mean latency of 2.3 ± 0.1 ms, a peak amplitude of 0.56 ± 0.01 mV, and a decay time constant of 80.1 ± 6.2 ms (40 connections; Fig. 1, E and F, and table S1). Unitary excitatory postsynaptic currents (EPSCs) had a mean latency of 2.2 ± 0.1 ms, a peak amplitude of 17.3 ± 2.0 pA, and a decay time constant of 9.5 ± 0.6 ms (39 connections; Fig. 1, G and H, and table S1). These results confirm and extend previous results in guinea-pig slices (15, 16).

Macroconnectivity in the CA3 network

Our results suggested that connectivity in the CA3 cell network was sparse, with a mean connection probability of 0.92%. Both experimental data and simulations using fully reconstructed CA3 neurons labeled *in vivo* indicated that connectivity was only moderately dependent on slice orientation (materials and methods; fig. S3). However, connectivity may decline with distance (17). Furthermore, connectivity might be nonrandom, with ensembles of highly connected cells embedded in a sparsely connected population (18, 19). To test these hypotheses, we first examined whether the connection probability was dependent on intersomatic distance (Fig. 2A). The average con-

nnection probability did not significantly change with distance, for intersomatic distances of up to 400 μm (Fig. 2A). Furthermore, both EPSP and EPSC peak amplitudes were not significantly dependent on distance (fig. S4, A and B).

Next, we examined whether synaptic connectivity was random. To test this, we counted all disynaptic connectivity motifs (reciprocal connections, convergent triples, divergent triples, and disynaptic chains) in our experimental data set and compared motif numbers to those of a simulated data set assuming random connectivity and a connection probability of 0.92% (i.e., the experimental value; Fig. 2, B and C). All disynaptic connectivity motifs occurred significantly more frequently than expected by chance. The frequency of reciprocal connections, convergent triples, divergent triples, and disynaptic chains was 6.5-, 2.9-, 6.3-, and 3.4-fold higher, respectively, than the corresponding chance level (Fig. 2C; $P \leq 0.002$ in all cases). Furthermore, we found several superconnectivity motifs (7 connections in one octuple, 10 and 3 connections in two septuples, and 3 connections in two quintuples), which were highly unlikely in random networks (Fig. 2D). As connection probability was not significantly dependent on intersomatic distance (Fig. 2A), the overabundance of motifs was not an epiphenomenon of distance dependence. Thus, connectivity in the CA3 cell network was not random, but highly enriched in connectivity motifs (17–19), reminiscent of a small-world network architecture (20). Both connection probability and abundance of motifs were similar in the range of ages tested (fig. S4, C and D). Comparison of properties of connections embedded in disynaptic motifs with those of isolated connections revealed that the EPSC peak amplitude was smaller and the proportion of failures was higher for embedded connections, whereas kinetic parameters were not significantly different (fig. S4E).

Microconnectivity of unitary CA3–CA3 connections

Next, we analyzed the microconnectivity between pairs of synaptically connected neurons (Fig. 3). Functionally connected cells were completely reconstructed, and putative synaptic contacts between presynaptic axons and postsynaptic dendrites were identified by light microscopy (Fig. 3A). In hippocampal CA3–CA3 cell synapses, connections were formed by only one or two putative synaptic contacts. One putative contact per connection was observed in 58% of functionally connected cells (7 out of 12 connections), and two synaptic contacts were observed in the remaining 42% of cases (5 out of 12 connections; Fig. 3C). Synapses were formed at equal proportions on the hilar (proximal) and the fimbrial (distal) side of the presynaptic neuron, suggesting uniformity along the CA3a–c axis (70 and 70 out of 140 connections; Fig. 3C). Putative synaptic contacts were located on basal dendrites in 53% of connections (9 out of 17 contacts) and on apical dendrites of postsynaptic target cells in the remaining 47% of cases (8 out of 17 contacts; Fig. 3C). On average, the dendritic distance of the putative contacts

¹IST Austria (Institute of Science and Technology Austria), Am Campus 1, A-3400 Klosterneuburg, Austria. ²Center for Molecular Neurobiology Hamburg, Falkenried 94, D-20251 Hamburg, Germany.
*Corresponding author. Email: peter.jonas@ist.ac.at

from the center of the soma of the postsynaptic target cell was $141 \pm 15 \mu\text{m}$ (12 reconstructed pairs; Fig. 3D). Thus, in contrast to the neocortex (21–23), synaptically interconnected CA3 pyramidal neurons showed only one or two morphological contacts per connection.

To determine the number of functional release sites and the corresponding release probability, we recorded EPSPs and EPSCs in physiological extracellular solution containing 2 mM Ca^{2+} , and in either reduced (1 mM) or elevated (4 mM) extracellular Ca^{2+} concentration (Fig. 3, E and

F). The entire peak amplitude data set was fit with a binomial release model in which quantal size and number of functional release sites were assumed to be the same for the two conditions, whereas release probability was specified separately (see materials and methods). Multiple probability binomial analysis revealed that the mean number of functional release sites was 3.2 ± 0.8 and that the corresponding release probability with a physiological extracellular Ca^{2+} concentration was 0.37 ± 0.04 (15 connections total; Fig. 3, E and F, and table S2). Thus, synaptic

transmission at CA3–CA3 synapses was mediated by few functional release sites with a relatively high release probability (24, 25). Hence, in contrast to the neocortex (21–23, 26), hippocampal CA3 pyramidal cells often communicated with each other via a small number of functional release sites.

Efficacy and summation of unitary synaptic events

The sparse connectivity in the CA3 cell network raises the question of how few CA3 pyramidal cells efficiently recruit their postsynaptic targets,

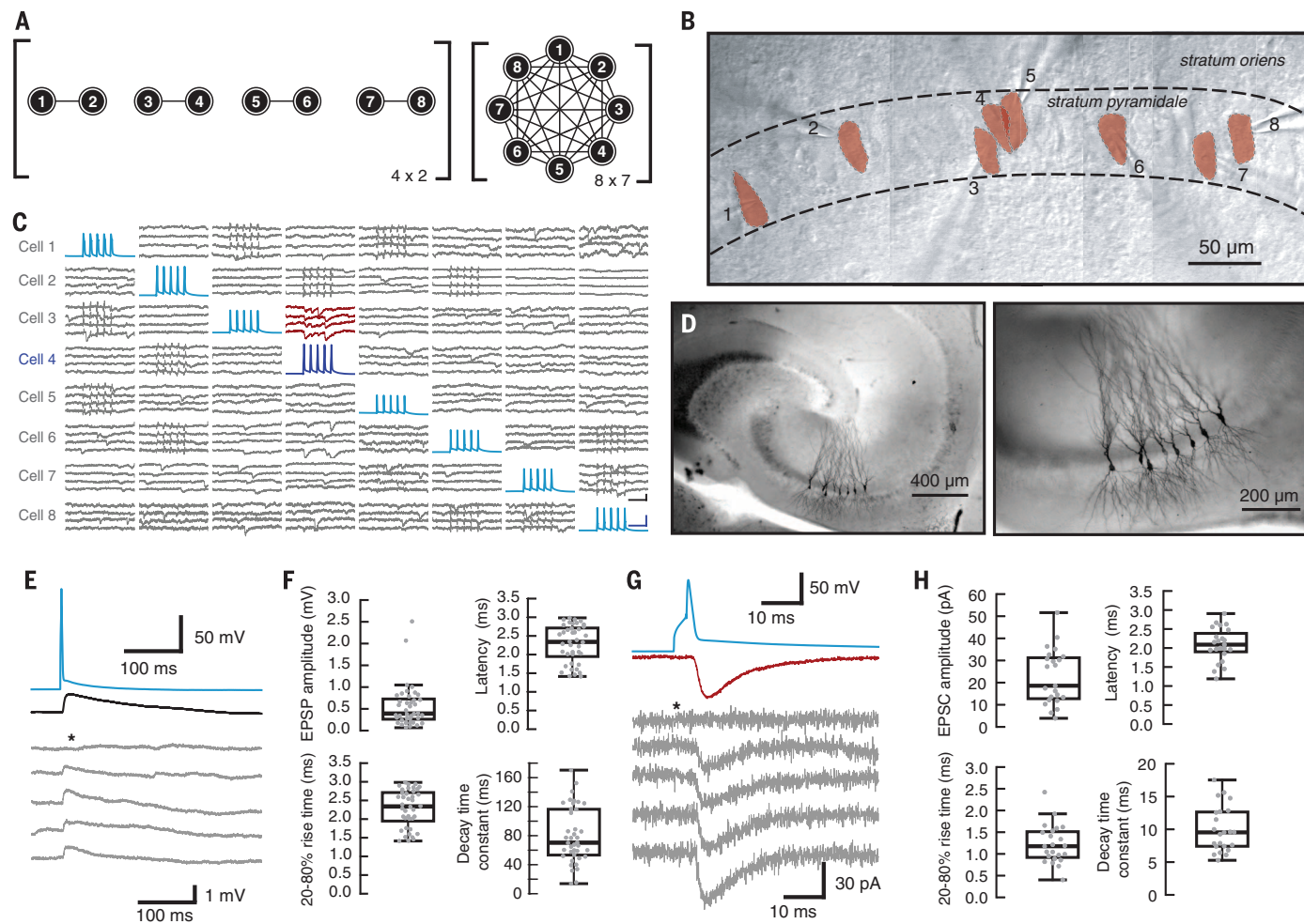


Fig. 1. Octuple recording in the CA3 cell network. (A) Advantage of the octuple recording configuration. In sequential paired recordings from eight cells (left), $4 \times 2 = 8$ potential connections can be examined. In a simultaneous octuple recording (right), $8 \times 7 = 56$ potential connections can be tested. (B) Infrared differential interference contrast videomicrograph of the hippocampal CA3b region in a thick-slice preparation, with eight recording electrodes attached to the somata of putative pyramidal neurons. Red areas represent the two-dimensional (2D) projections of cell bodies. (C) Functional connectomics in the CA3 pyramidal neuron network. Each column represents single traces from eight cells; number code as shown in (B). In each of the eight columns, a different cell was stimulated by a series of five current pulses in current-clamp (blue traces), while the other cells were recorded in the voltage-clamp configuration (gray traces). In this octuple recording, cell 4 (dark blue trace) was connected to cell 3 (red traces). In this octuple recording, cell 4 (dark blue trace) was connected to cell 3 (red traces). Scale bars, 50 mV or 10 pA, 10 ms (bottom, right). Brief transients in a subset of traces represent capacitive coupling artifacts, as reported in previous publications [e.g., (47)]. (D) Light micrograph

of a biocytin-labeled octuple (maximal intensity projection stack; left panel, low magnification; right panel, high magnification). Eight CA3 pyramidal neurons in area CA3b were filled with biocytin during whole-cell recording and labeled with 3,3'-diaminobenzidine as chromogen. Data in (B) to (D) were obtained from different octuples. For the octuple shown in (D), all eight cells were labeled with biocytin for illustration purposes, i.e., selective labeling (fig. S1) was not performed. (E and F) Properties of unitary EPSPs at CA3–CA3 synapses. (E) Representative traces. Top, presynaptic action potential; center, average EPSP; bottom, individual EPSPs. (F) Summary graphs of EPSP peak amplitude, latency, 20 to 80% rise time, and decay time constant. (G and H) Similar graphs to those in (E) and (F), but for EPSCs. Asterisks in (E) and (G) indicate failures. In box plots, horizontal lines represent median; boxes, quartiles; whiskers, most extreme data points ≤ 1.5 interquartile range from box edges; and single points, data from individual experiments. Throughout this Article, presynaptic action potentials are shown in blue, EPSPs in black, and EPSCs in red.

as required for pattern completion. To address this question, we explored the properties of unitary postsynaptic conductance (Fig. 4). To estimate peak amplitude and time course of the postsynaptic conductance in the dendrite, we first determined the location of putative synaptic contacts in post-hoc labeled pairs. We then reconstructed the somatodendritic morphology of the postsynaptic CA3 pyramidal neuron and converted it into a detailed cable model (Fig. 4A). Finally, we simulated EPSCs, varying latency, rise time constant, peak amplitude, and decay time constant of the postsynaptic conductance until the best fit of the experimentally recorded average somatic EPSCs was obtained. Experimentally constrained modeling revealed a rise time constant of 0.26 ± 0.07 ms, a peak conductance of 0.54 ± 0.12 nS, and a decay time constant of 6.71 ± 1.46 ms (10 connections; Fig. 4, B and C). Considering the single-channel conductance of dendritic AMPARs in CA3 pyramidal neurons (10 pS) (27) and a mean number of 3.2 functional release sites (Fig. 3F), this peak conductance corresponded to 17 AMPARs per site open at the peak of an EPSC (28). Thus, a large number of postsynaptic

AMPARs contributed to synaptic efficacy at recent CA3–CA3 synapses.

Because a single unitary EPSP could not fire a postsynaptic CA3 cell (Fig. 1, E and F), we next examined the rules of temporal and spatial summation. To quantify temporal summation, we measured EPSPs evoked by repetitive stimulation of the presynaptic cell, using high-frequency trains of five or ten stimuli (Fig. 4D), which mimics burst activity of CA3 pyramidal cells in vivo (29). EPSPs showed substantial summation during repetitive stimulation. For 20-, 50-, and 100-Hz trains of five presynaptic action potentials, the ratio of $EPSP_{max}/EPSP_1$ was 1.58 ± 0.28 , 2.25 ± 0.49 , and 5.17 ± 2.50 , respectively (3, 10, and 4 connections). Thus, for high-frequency stimulation, temporal summation was nearly linear, with a maximal depolarization proportional to the number of spikes in the presynaptic neuron. Both the slow decay time constant of EPSPs (Fig. 1, E and F, and table S1) and the minimal synaptic depression during repetitive stimulation (fig. S5) contributed to efficient temporal summation.

To probe spatial summation, we stimulated two presynaptic cells converging on the same

postsynaptic neuron. Costimulation of the presynaptic cells with 50-Hz trains of stimuli led to compound EPSPs almost indistinguishable from the arithmetic sum of individual unitary EPSPs (Fig. 4D). Thus, spatial summation had approximately linear characteristics (30, 31). To determine the number of convergent presynaptic inputs necessary to drive the cell to firing threshold, we plotted the depolarization evoked by train stimulation against the number of stimulated inputs, and determined the number of inputs required for spiking from the intersection of a regression line with the action potential threshold (Fig. 4, E and F, and table S1). With a mean resting potential of -68.2 ± 1.0 mV and a mean action potential voltage threshold of -36.1 ± 1.6 mV, we estimated that 7.3 ± 1.9 coactive convergent inputs were required to initiate action potentials in a postsynaptic CA3 cell for 50-Hz stimulation. In the presence of ongoing synaptic activity in vivo, we estimated that 3.3 inputs would be required (29). Thus, the large number of postsynaptic AMPARs and the efficient temporal and spatial summation underlie the efficacy of synaptic signaling at CA3–CA3 pyramidal neuron synapses.

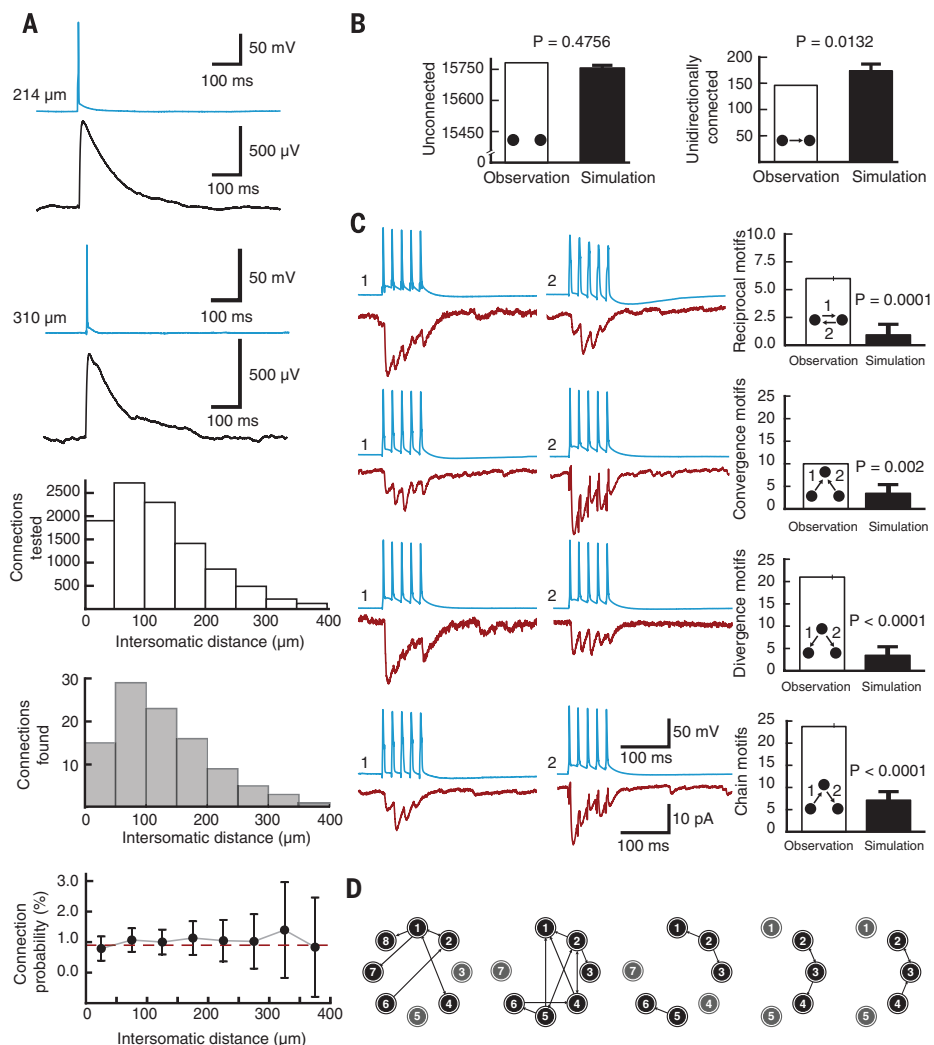


Fig. 2. Macroconnectivity of the CA3 cell network: Sparse and spatially uniform connectivity with overabundance of connectivity motifs.

(A) Analysis of dependence of connection probability on intersomatic distance. Top, traces of action potentials and average unitary EPSPs at two different distances (214 and 310 μm). Center, histogram of number of connections tested (white bars) and functional connections detected (gray bars). Bottom, connection probability, determined as the ratio of connections detected to connections tested, plotted versus distance. Error bars represent 95% confidence intervals estimated from a binomial distribution. Red dashed line indicates the mean connection probability (0.92%). (B) Number of unconnected and unidirectionally connected pairs. Bar graphs show the number of a given motif in the experimental sample (open bars) and the predicted number in a network with random connectivity and mean connection probability of 0.92% (filled bars). Data from 10,000 simulations; error bars indicate SD. (C) Overabundance of disynaptic connectivity motifs: reciprocally connected pairs, convergence motifs, divergence motifs, and chains (from top to bottom). Left, traces of action potentials and average unitary EPSCs. Right, summary bar graphs. *P* values are indicated above the simulation bar. The probability of experimentally observed connectivity motifs was significantly higher than expected by chance. (D) Detailed maps of super-connectivity motifs in our data set (7 connections in one octuple; 10 and 3 connections in two septuples; 3 connections in two quintuples). The probability that such connectivity motifs occur by chance is negligibly small.

Biologically constrained network models of pattern completion

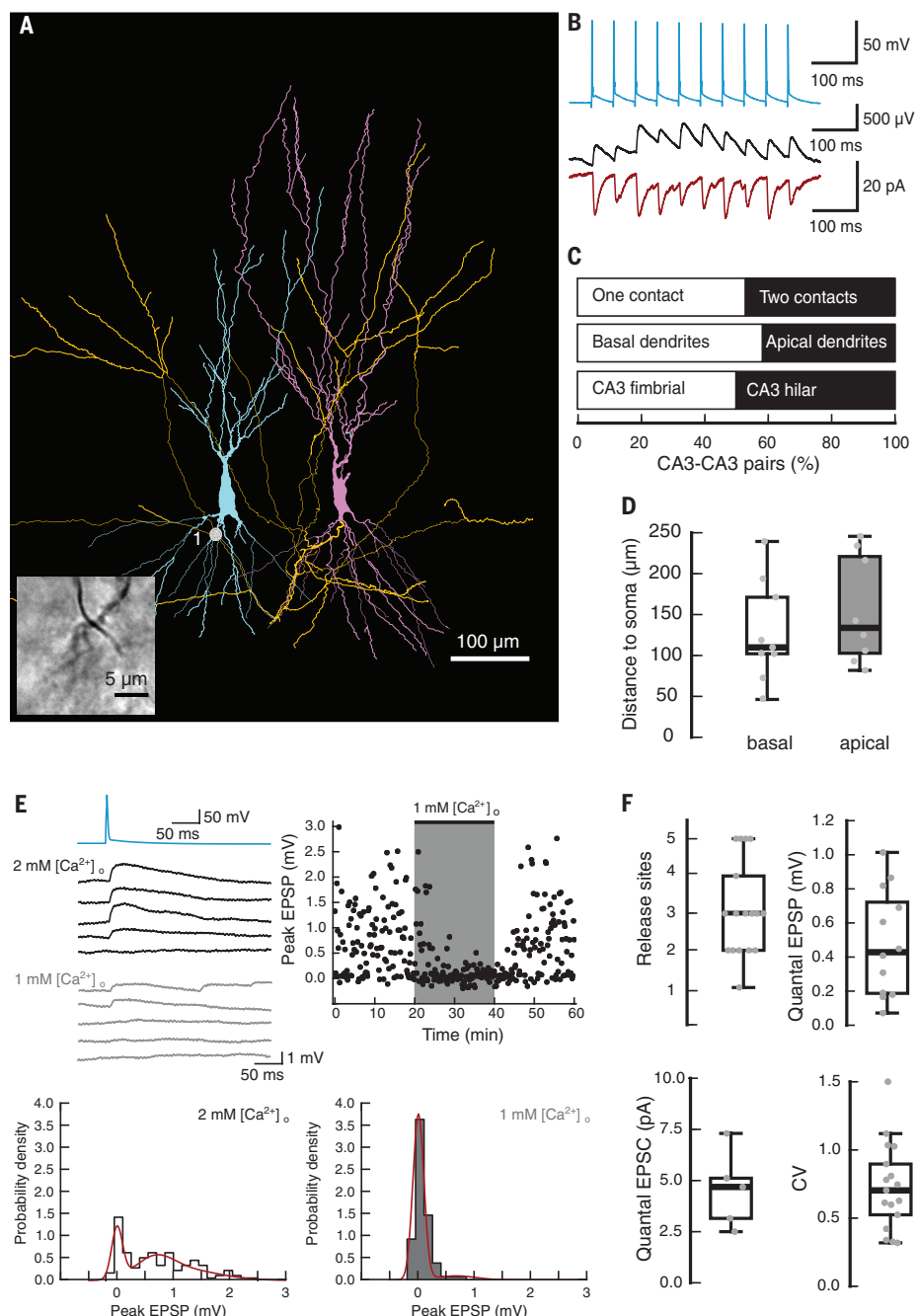
The present experimental findings challenged several assumptions of previous pattern completion models (3–5, 9, 14). First, the low average connectivity may compromise pattern completion. Second, the small number of synaptic contacts per connection will introduce synaptic noise, which may impair pattern completion (14). To examine how the experimentally determined properties of CA3–CA3 cell synapses affect pattern completion, we developed a real-size model of the hippocampal CA3 cell network (Fig. 5). The total number of neurons was 330,000, representing the

CA3 network of one hemisphere (32). Synaptic plasticity was implemented according to a clipped Hebbian rule (8), in agreement with recent experimental results at CA3–CA3 synapses (33). The firing threshold was set according to the observation that ≥3 synaptic inputs were necessary to activate a postsynaptic neuron (Fig. 4F) (29). An increasing number of random patterns was stored in the network, and recall was tested with degraded patterns (see materials and methods, fig. S6, and table S3). We first examined a network with a connection probability (p) of 3% and an activity level (f) of 0.001 (i.e., 330 active neurons per pattern). Such a network model produced

robust pattern completion (capacity ~45,000 patterns; Fig. 5B, left). Variation of the activity level confirmed that $f = 0.001$ provided favorable conditions for recall (fig. S7), as previously suggested (14).

Next, we examined how macroconnectivity affected pattern completion. When the connection probability in a random network was reduced, pattern completion was impaired ($p = 1.5\%$; Fig. 5B, center) or completely abolished ($p = 1\%$; Fig. 5B, right). Increasing the activity level ($f = 0.002$) partially rescued pattern completion (capacity ~8200 patterns; Fig. 5C, left), although recall was only possible in a narrow range of

Fig. 3. Microconnectivity of the CA3 cell network: A small number of morphological contacts and functional release sites per unitary connection. (A) Digital reconstruction of a functionally connected CA3–CA3 pair based on the post-hoc biocytin labeling. Soma and dendrites of presynaptic cell are shown in magenta, axon of presynaptic cell is in yellow, soma and dendrites of postsynaptic cell are in cyan. Gray dot indicates putative synaptic contact; inset shows light micrograph of the contact. (B) Unitary EPSPs and EPSCs from the same morphologically reconstructed neuron. Upper traces represent presynaptic action potentials, center traces average unitary EPSPs, and bottom traces average unitary EPSCs. (C) Summary bar graphs of number of putative contacts per connection (top), number of contacts on basal versus apical dendrites (center), and number of contacts on the fimbrial = distal versus hilar = proximal regions (from the perspective of the presynaptic neuron). (D) Dendritic distance of putative contacts on the basal (left) and the apical (right) dendrites of the postsynaptic cell. (E) A small number of functional release sites revealed by changing the extracellular Ca^{2+} concentration. Top left, single EPSP traces during standard (2 mM Ca^{2+} , black) and low-release probability conditions (1 mM Ca^{2+} , gray). Top right, plot of EPSP peak amplitude against experimental time at CA3–CA3 synapses during reduction of the extracellular Ca^{2+} concentration (gray area). Bottom, histogram of EPSP peak amplitude under standard (2 mM Ca^{2+} , left) and low-release probability conditions (1 mM Ca^{2+} , right). Red curve shows the results of multiple probability binomial analysis. Changing the extracellular Ca^{2+} concentration markedly altered the proportion of failures and successes, but had relatively small effects on the amplitude of successes, suggesting a small number of functional release sites. (F) Summary graph of number of release sites (top, left), quantal EPSP amplitude (top, right), quantal EPSC amplitude (bottom, left), and coefficient of variation (bottom, right). In box plots, horizontal lines represent median; boxes, quartiles; whiskers, most extreme data points ≤ 1.5 interquartile range from box edges; and single points, data from individual experiments.



inhibition. Incorporation of reciprocal, convergence, divergence, and chain motifs (34) also rescued pattern completion (capacity ~3600 patterns; Fig. 5C, center); recall was possible over a wide range of inhibition. Addition of reciprocal, convergence, and divergence motifs (i.e., all except chain motifs) failed to rescue pattern completion, showing that chain motifs played a critical role (Fig. 5C, right; fig. S8). Incorporation of all motifs also rescued pattern completion for $p = 1.5\%$, but reduced capacity for $p = 3\%$ (fig. S9), showing that motifs selectively enhanced network performance in combination with sparse connectivity. Similar conclusions were reached in network models with limited projection along the longitudinal axis (35, 36) (fig. S10) and in network models with $2 \times 330,000$ neurons and contralateral projections (fig. S11, A and B). In contrast, pattern completion was impaired in network models with $1/3 \times 330,000$ neurons, suggesting that isolated CA3b subnetworks were insufficient for pattern completion (fig. S11, C and D).

Finally, we tested how microconnectivity affected pattern completion. Two opposite predictions can be made. First, increasing the number of synaptic contacts per connection will reduce the coefficient of variation (CV) of synaptic transmission, which may enhance pattern completion (14). Second, increasing the number of contacts per connection would reduce the effective connectivity, because presynaptic terminals have to compete for space on dendritic spines of postsynaptic target cells. This may decrease network capacity (Fig. 5B). To assess the relative importance of these effects, we introduced synaptic variability in our simulations. With a connection probability of 3% and a CV of 1, pattern completion worked reliably (capacity ~7000 patterns; Fig. 5D, center). Reducing the CV improved pattern completion (capacity ~22,000 patterns; Fig. 5D, left). However, reducing CV and connectivity in combination abolished pattern completion (capacity close to 0; Fig. 5D, right). Therefore, single-contact synapses with high variability were

better suited for pattern completion than multi-contact synapses with low variability.

Discussion

Previous theories of the hippocampal formation often depicted the CA3 region as a network of highly interconnected cells, in which connectivity is all-to-all, random, or distance dependent (3–5, 8, 9, 11, 14, 37). Our experimental results challenge this view in multiple ways. First, the macroconnectivity in the CA3 cell network is sparse, spatially uniform, and highly enriched in disynaptic connectivity motifs. This is different from the neocortex, where connection probability is higher (~10%), more distance dependent, and less enriched in disynaptic motifs (17, 18, 22, 38). Second, the microconnectivity in individual CA3-CA3 connections is characterized by a small number of synaptic contacts and functional release sites per connection. Again, this is different from the neocortex, where unitary synaptic interactions involve a large number of contacts (up to eight in

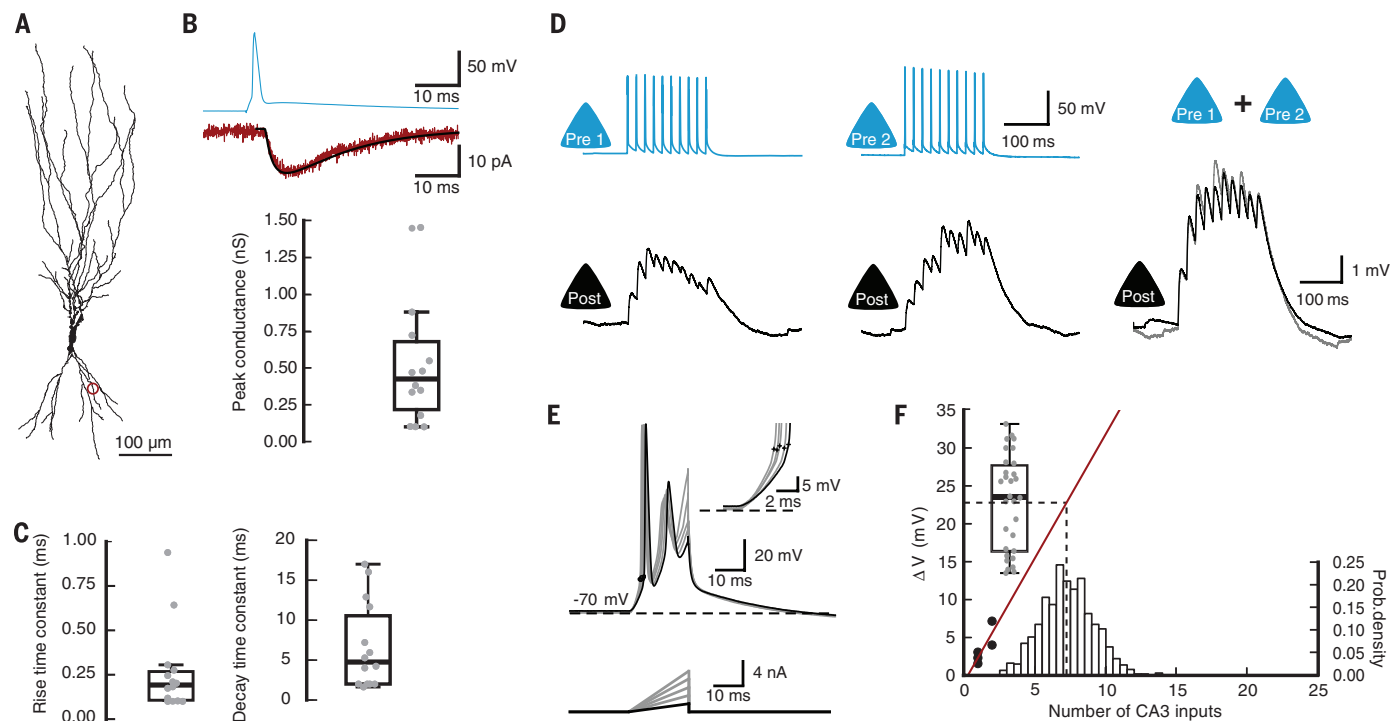
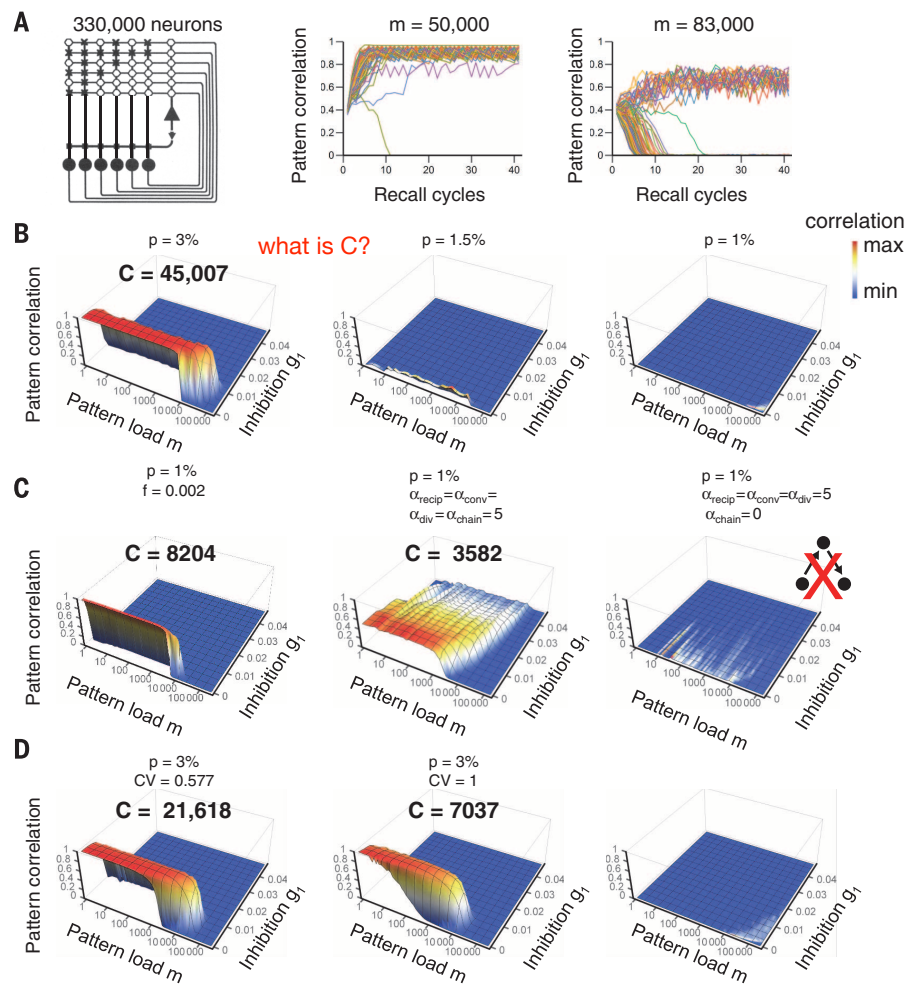


Fig. 4. Synaptic efficacy at recurrent CA3-CA3 synapses: Large post-synaptic conductance and efficient summation. (A) Analysis of postsynaptic conductance. Digital reconstruction of soma and dendrites of the postsynaptic cell in a synaptically connected CA3-CA3 pair based on the post-hoc biocytin labeling. Red circle indicates the putative synaptic contact. (B) Unitary EPSCs and estimated peak conductance. Latency, rise time constant, peak amplitude, and decay time constant were fit as free parameters. Top, presynaptic action potential and average EPSC (red trace), superimposed with the results of the postsynaptic conductance fit (black curve). Bottom, summary graph of peak conductance. (C) Rise time and decay time constant of the postsynaptic conductance. (D) Efficient temporal and spatial summation at CA3-CA3 synapses. Left, EPSPs evoked by repetitive stimulation of the presynaptic neuron (10 stimuli applied at a frequency of 50 Hz). Center, EPSPs evoked by repetitive stimulation of another presynaptic neuron converging on the same postsynaptic cell. Right, EPSPs evoked by simultaneous repetitive stimulation of both presynaptic neurons.

(black), superimposed with the arithmetic sum of the individual responses (gray). The two curves superimpose, indicating linear summation. In left and center subpanels, the top trace shows the presynaptic action potential, and the bottom trace represents the average EPSP. (E) Analysis of voltage threshold of action potential initiation. A ramp protocol was used to determine the action potential voltage threshold (criterion 20 V s^{-1} , small crosses). (F) Plot of summed EPSP amplitude (50 Hz stimulation) against number of stimulated inputs (black circles). Voltage threshold values are shown for comparison (gray circles). Continuous red line indicates the results of linear regression of summation data. Dashed lines indicate mean number of inputs required to fire a postsynaptic CA3 pyramidal cell and the corresponding mean action potential threshold value. Histogram depicts the distribution of the estimated number of inputs required to fire the postsynaptic cell under *in vitro* conditions. In box plots, horizontal lines represent median; boxes, quartiles; whiskers, most extreme data points ≤ 1.5 interquartile range from box edges; and single points, data from individual experiments.

Fig. 5. Pattern completion in a CA3 network model with sparse connectivity, disynaptic connectivity motifs, and single-contact synapses. (A) Left, schematic illustration of network topology. Large filled circles, principal neurons; large filled triangle, inhibitory interneuron; small open circles, potentiated synapses; small crosses, unpotentiated synapses. Center, correlation between actual and stored patterns, plotted against the number of the recall cycle. Pattern load was $m = 50,000$ (center) and $83,000$ (right), respectively; connection probability $p = 3\%$; inhibition factor $g_1 = 0.0072$; random connectivity in both cases. Lines with different colors represent trajectories for 100 random patterns. (B) Dependence of pattern completion in an autoassociative memory network model on network connectivity. Connection probability was $p = 3\%$ [left; corresponding plot of pattern correlation against recall cycle shown in (A)], 1.5% (center), and 1% (right); random connectivity in all cases; average activity level $f = 0.001$. The 3D plots indicate average correlation between original patterns and retrieved patterns, plotted against pattern load (m) and inhibition factor (g_1). Height of the correlation plot is color coded, with red representing maximal and blue minimal correlation (see pseudocolor scale bar on top right). Performance of the pattern completion network was high for a connection probability of 3% , but declined as connectivity was reduced. (C) Increasing activity and introducing connectivity motifs rescued pattern completion in sparsely connected networks. A 3D plot of correlation against pattern load (m) and inhibition factor (g_1). Left, $p = 1\%$ combined with increased activity ($f = 0.002$). Center, $p = 1\%$ combined with high abundance of motifs ($\alpha_{\text{recip}} = \alpha_{\text{conv}} = \alpha_{\text{div}} = \alpha_{\text{chain}} = 5$). Right, $p = 1\%$ combined with selective elimination of chain motifs ($\alpha_{\text{recip}} = \alpha_{\text{conv}} = \alpha_{\text{div}} = 5$; $\alpha_{\text{chain}} = 0$). α quantifies how much the frequency of a motif exceeds the corresponding value for a random network. (D) Reducing the CV and connection probability, as may occur during the transition from single-contact to multicontact synapses, alters network performance. Center, synaptic CV = 1, connection probability $p = 3\%$. Left, effects of reducing CV without change in effective connectivity ($\text{CV} = 1/\sqrt{3} = 0.577$; $p = 3\%$). Right, effects of correlated changes of CV and effective connectivity, with the total number of synapses kept constant ($\text{CV} = 1/\sqrt{3} = 0.577$; $p = 1\%$). Random connectivity in all cases; average activity level $f = 0.001$. The effects of connectivity dominated over those of CV. All simulations were performed with the real-size network (330,000 neurons with standard parameters). Sparse activity ($f = 0.001$) in all cases except panel C, left. For details, see materials and methods and table S3.



Downloaded from <http://science.sciencemag.org/> on October 7, 2018

layer 5–layer 5 pyramidal neuron pairs) (21–23, 26). Finally, despite the small number of synaptic contacts, the efficacy of unitary connections is high. Therefore, coincident firing of a small number of presynaptic cells is sufficient to initiate action potentials in a postsynaptic cell. Thus, the properties of recurrent CA3–CA3 synapses allow efficient encoding of information by small neuronal ensembles.

Our results give important insights into the synaptic mechanisms of pattern completion. First, they provide a proof of principle that real-size networks with a realistic connection probability of 1% can perform pattern completion. Second, they demonstrate that connectivity motifs increase the efficacy and robustness of recall under conditions of sparse connectivity and sparse activity. Intuitively, incorporation of motifs will increase the variance in the number of inputs and outputs of each cell, which will facilitate the spread of activity in the network and thereby enhance the robustness of recall (14). Finally, they

suggest that the design of CA3–CA3 synapses with few synaptic contacts per connection is favorable, because it enables maximally efficient use of postsynaptic space. Thus, both macro- and microconnectivity facilitate pattern completion in the CA3 cell network. Similar conclusions were independently reached in a theoretical study, which deduced sparse connectivity and high motif abundance from the assumption of maximal storage capacity (39).

The mechanisms generating the motif structure are currently unknown. Anisotropy of axonal connections may contribute, but it is unlikely to be the only factor. One possibility is that connectivity motifs are formed during development, connecting clonally related groups of sister cells (40, 41). Alternatively, the motifs may arise from structural plasticity in synchronously active neuronal ensembles (33, 42). Because mossy fiber synapses may “detonate” postsynaptic CA3 pyramidal neurons (43, 44), CA3 neurons innervated by the same mossy fiber axon might become preferen-

tially connected through activity-dependent synaptic plasticity. This would provide a structured connection between pattern separation circuits of the dentate gyrus and pattern completion networks of the CA3 region (37). Similarly, CA3 neurons targeted by the same entorhinal inputs could become connected. Finally, the CA3 connectome may be altered during chronic inactivity (45) or brain diseases (46). How this would affect pattern completion in the network remains to be determined.

REFERENCES AND NOTES

- H. Eichenbaum, *Neuron* **44**, 109–120 (2004).
- R. P. Kesner, *Learn. Mem.* **14**, 771–781 (2007).
- B. L. McNaughton, R. G. M. Morris, *Trends Neurosci.* **10**, 408–415 (1987).
- A. Treves, E. T. Rolls, *Hippocampus* **4**, 374–391 (1994).
- J. E. Lisman, *Neuron* **22**, 233–242 (1999).
- K. Nakazawa, T. J. McHugh, M. A. Wilson, S. Tonegawa, *Nat. Rev. Neurosci.* **5**, 361–372 (2004).
- J. P. Neunuebel, J. J. Knierim, *Neuron* **81**, 416–427 (2014).

8. D. J. Willshaw, O. P. Buneman, H. C. Longuet-Higgins, *Nature* **222**, 960–962 (1969).
9. D. Marr, *Philos. Trans. R. Soc. Lond. B Biol. Sci.* **262**, 23–81 (1971).
10. G. Palm, *Biol. Cybern.* **36**, 19–31 (1980).
11. J. J. Hopfield, *Proc. Natl. Acad. Sci. U.S.A.* **79**, 2554–2558 (1982).
12. H. Sompolinsky, *Phys. Rev. A Gen. Phys.* **34**, 2571–2574 (1986).
13. D. J. Amit, H. Gutfreund, H. Sompolinsky, *Phys. Rev. A* **35**, 2293–2303 (1987).
14. M. R. Bennett, W. G. Gibson, J. Robinson, *Philos. Trans. R. Soc. Lond. B Biol. Sci.* **343**, 167–187 (1994).
15. R. Miles, R. K. S. Wong, *J. Physiol.* **373**, 397–418 (1986).
16. R. D. Traub, R. Miles, *Neuronal Networks of the Hippocampus*. (Cambridge Univ. Press, Cambridge, 1991).
17. R. Perin, T. K. Berger, H. Markram, *Proc. Natl. Acad. Sci. U.S.A.* **108**, 5419–5424 (2011).
18. S. Song, P. J. Sjöström, M. Reigl, S. Nelson, D. B. Chklovskii, *PLOS Biol.* **3**, e68 (2005).
19. S. Rieubland, A. Roth, M. Häusser, *Neuron* **81**, 913–929 (2014).
20. D. J. Watts, S. H. Strogatz, *Nature* **393**, 440–442 (1998).
21. J. Lübke, H. Markram, M. Frotscher, B. Sakmann, *J. Neurosci.* **16**, 3209–3218 (1996).
22. H. Markram, J. Lübke, M. Frotscher, A. Roth, B. Sakmann, *J. Physiol.* **500**, 409–440 (1997).
23. T. Branco, K. Staras, *Nat. Rev. Neurosci.* **10**, 373–383 (2009).
24. A. I. Gulyás et al., *Nature* **366**, 683–687 (1993).
25. N. Holderith et al., *Nat. Neurosci.* **15**, 988–997 (2012).
26. R. A. Silver, J. Lübke, B. Sakmann, D. Feldmeyer, *Science* **302**, 1981–1984 (2003).
27. N. Spruston, P. Jonas, B. Sakmann, *J. Physiol.* **482**, 325–352 (1995).
28. Z. Nusser et al., *Neuron* **21**, 545–559 (1998).
29. J. Kowalski, J. Gan, P. Jonas, A. J. Pernia-Andrade, *Hippocampus* **26**, 668–682 (2016).
30. S. Cash, R. Yuste, *Neuron* **22**, 383–394 (1999).
31. S. Kim, S. J. Guzman, H. Hu, P. Jonas, *Nat. Neurosci.* **15**, 600–606 (2012).
32. D. G. Amaral, N. Ishizuka, B. Claiborne, *Prog. Brain Res.* **83**, 1–11 (1990).
33. R. K. Mishra, S. Kim, S. J. Guzman, P. Jonas, *Nat. Commun.* **7**, 11552 (2016).
34. L. Zhao, B. Beverlin 2nd, T. Netoff, D. Q. Nykamp, *Front. Comput. Neurosci.* **5**, 28 (2011).
35. X. G. Li, P. Somogyi, A. Ylinen, G. Buzsáki, *J. Comp. Neurol.* **339**, 181–208 (1994).
36. M. P. Witter, *Learn. Mem.* **14**, 705–713 (2007).
37. E. T. Rolls, *Front. Syst. Neurosci.* **7**, 74 (2013).
38. S. Lefort, C. Tomm, J. C. Floyd Sarria, C. C. Petersen, *Neuron* **61**, 301–316 (2009).
39. N. Brunel, *Nat. Neurosci.* **19**, 749–755 (2016).
40. Y. Deguchi, F. Donato, I. Galimberti, E. Cabuy, P. Caroni, *Nat. Neurosci.* **14**, 495–504 (2011).
41. Y. C. Yu, R. S. Bultje, X. Wang, S. H. Shi, *Nature* **458**, 501–504 (2009).
42. F. Engert, T. Bonhoeffer, *Nature* **399**, 66–70 (1999).
43. D. A. Henze, L. Wittner, G. Buzsáki, *Nat. Neurosci.* **5**, 790–795 (2002).
44. N. P. Vyleta, P. Jonas, *Science* **343**, 665–670 (2014).
45. A. Mitra, S. S. Mitra, R. W. Tsien, *Nat. Neurosci.* **15**, 250–257 (2012).
46. J. E. Hanson, M. Blank, R. A. Valenzuela, C. C. Garner, D. V. Madison, *J. Physiol.* **579**, 53–67 (2007).
47. J. J. Couey et al., *Nat. Neurosci.* **16**, 318–324 (2013).

ACKNOWLEDGMENTS

We thank A. Aertsen, J. Csicsvari, A. Roth, C. Savin, R. Shigemoto, and two anonymous reviewers for critically reading the manuscript, as well as J. Szabadics and S. Rotter for useful discussions. We are grateful to F. Marr for excellent technical assistance, B. Joch for help with morphological analysis, E. Kramberger for manuscript editing, T. Asenov (Miba machine shop) for technical support, and M. Schunn (preclinical facility) for animal maintenance. We also thank the scientific computing facilities, University of Innsbruck, for help with the MACH computer cluster. Finally, we thank D. Nykamp for providing programs and G. Buzsáki,

L. Wittner, G. Ascoli, and D. Ropireddy for sharing CA3 pyramidal neuron models. Supported by the Fond zur Förderung der Wissenschaftlichen Forschung (P 24909-B24 to P.J.), the European Union (European Research Council Advanced Grant 268548 to P.J.), and the Deutsche Forschungsgemeinschaft (FR 620/14-1 to M.F.). M.F. is Senior Research Professor of the Hertie Foundation. The authors declare no conflicts of interest. Original data and programs were stored in the scientific repository of the Institute of Science and Technology Austria and are available on request.

SUPPLEMENTARY MATERIALS

www.sciencemag.org/content/353/6304/1117/suppl/DC1
Materials and Methods
Figs. S1 to S11
Tables S1 to S4
References (48–68)

3 January 2016; accepted 15 July 2016
10.1126/science.aaf1836

INHIBITORY SYNAPSES

Identification of an elaborate complex mediating postsynaptic inhibition

Akiyoshi Uezu,¹ Daniel J. Kanak,^{1*} Tyler W. A. Bradshaw,^{1*} Erik J. Soderblom,^{1,2} Christina M. Catavero,¹ Alain C. Burette,^{3,4} Richard J. Weinberg,^{3,4} Scott H. Soderling^{1,5,†}

Inhibitory synapses dampen neuronal activity through postsynaptic hyperpolarization. The composition of the inhibitory postsynapse and the mechanistic basis of its regulation, however, remain poorly understood. We used an *in vivo* chemico-genetic proximity-labeling approach to discover inhibitory postsynaptic proteins. Quantitative mass spectrometry not only recapitulated known inhibitory postsynaptic proteins but also revealed a large network of new proteins, many of which are either implicated in neurodevelopmental disorders or are of unknown function. Clustered regularly interspaced short palindromic repeats (CRISPR) depletion of one of these previously uncharacterized proteins, InSyn1, led to decreased postsynaptic inhibitory sites, reduced the frequency of miniature inhibitory currents, and increased excitability in the hippocampus. Our findings uncover a rich and functionally diverse assemblage of previously unknown proteins that regulate postsynaptic inhibition and might contribute to developmental brain disorders.

Two anatomically distinct classes of synapses are present in the central nervous system: excitatory synapses, predominantly localized to postsynaptic spines, and inhibitory synapses, in which the postsynapse is typically embedded in the soma and dendritic shaft (1). Purification and analysis of the protein complexes of the excitatory postsynapse have led to fundamental insights in neurobiology. These insights include how receptor trafficking, synaptic adhesion, cytoskeletal remodeling, and protein phosphorylation contribute to the synaptic plasticity underlying learning and memory (2, 3). Moreover, genetic perturbations of excitatory postsynaptic proteins are strongly implicated in developmental brain disorders and psychiatric conditions (4, 5).

In contrast, the biochemical purification and analysis of the inhibitory postsynaptic density (iPSD) has remained largely intractable. Accordingly, the molecular basis of postsynaptic inhibitory synapse regulation and its contribution to neurodevelopmental disorders is poorly understood. Recently, an affinity purification approach,

BioID, has been developed that utilizes a promiscuous *Escherichia coli* biotinylation enzyme BirA^{Arg118G} (here termed BirA, with Gly replacing Arg¹¹⁸) fused to a bait protein expressed in cells (6). BirA-dependent covalent biotinylation occurs within 10 to 50 nm of the bait protein and allows for efficient isolation and analysis of proximal proteins by streptavidin-based affinity purification and mass spectrometry (MS) (7). Compared with affinity purification methods, the BioID reaction is executed *in situ* and thus enables the capture of protein complexes, including transient interactions and insoluble proteins from subcellular compartments refractory to biochemical isolation (8).

We adapted the proximity-dependent biotin identification (BioID) approach to enable *in vivo* BioID (iBioID) of synaptic complexes in mouse brain. We virally expressed inhibitory or excitatory PSD proteins fused to BirA to capture and purify their associated proteins. The method labels the corresponding postsynaptic structures *in vivo*, and that enabled the identification of virtually all of the known proteins of the iPSD. It also revealed a large number of previously unknown proteins, including a rich diversity of transmembrane and signaling proteins. These results provide a molecular prospectus for the deeper understanding of synaptic physiology that was, until now, largely confined to the excitatory PSD.

In vivo capture of synaptic protein complexes

Gephyrin is the major scaffolding protein organizing the iPSD structure, interacting directly with

¹The Department of Cell Biology, Duke University Medical School, Durham, NC 27703, USA. ²Duke Proteomics and Metabolomics Shared Resource and Duke Center for Genomic and Computational Biology, Duke University Medical School, Durham, NC 27703, USA. ³Department of Cell Biology and Physiology, University of North Carolina, Chapel Hill, NC 27599, USA. ⁴Neuroscience Center, University of North Carolina, Chapel Hill, NC 27599, USA.

⁵The Department of Neurobiology, Duke University Medical School, Durham, NC 27703, USA.

*These authors contributed equally to this work. †Corresponding author: Email: scott.soderling@duke.edu

Synaptic mechanisms of pattern completion in the hippocampal CA3 network

Segundo Jose Guzman, Alois Schlägl, Michael Frotscher and Peter Jonas

Science 353 (6304), 1117-1123.
DOI: 10.1126/science.aaf1836

ARTICLE TOOLS

<http://science.scienmag.org/content/353/6304/1117>

SUPPLEMENTARY MATERIALS

<http://science.scienmag.org/content/suppl/2016/09/07/353.6304.1117.DC1>

REFERENCES

This article cites 65 articles, 12 of which you can access for free
<http://science.scienmag.org/content/353/6304/1117#BIBL>

PERMISSIONS

<http://www.scienmag.org/help/reprints-and-permissions>

Use of this article is subject to the [Terms of Service](#)

Science (print ISSN 0036-8075; online ISSN 1095-9203) is published by the American Association for the Advancement of Science, 1200 New York Avenue NW, Washington, DC 20005. 2017 © The Authors, some rights reserved; exclusive licensee American Association for the Advancement of Science. No claim to original U.S. Government Works. The title *Science* is a registered trademark of AAAS.